Highlights

- Development of neural networks for homogenization of periodic microstructures
- Direct integration of elasticity solutions into the neural network architecture
- Application of transfer learning to train new microstructures from pre-trained model

Micromechanics-Informed Neural Networks for Periodic Homogenization of Thermocondcutive Behavior in Unidirectional Composites with Cylindrically Orthotropic Graphite Fibers

Ce Xiao[a,b], Qiang Chen[a,b*], Mohammed El Fallaki Idrissi[c], Zhibo Yang[a,b], Xuefeng Chen[a,b], George Chatzigeorgiou[c], Fodil Meraghni[c]

[a]National Key Lab of Aerospace Power System and Plasma Technology, Xi'an Jiaotong University, 710049 Xi'an, China

[b] School of Mechanical Engineering, Xi'an Jiaotong University, Xi'an 710049, Shaanxi, China

[c] Arts et Métiers Institute of Technology, CNRS, Université de Lorraine, LEM3-UMR7239, F-57000 Metz, France

* Corresponding author: qiangchen@xjtu.edu.cn

Abstract

A micromechanics-informed neural network framework is developed for homogenization of periodic unidirectional thermoconductive composites with cylindrically orthotropic fibers. The framework hard-imposes the steady-state governing heat conduction equations within the network architecture, enabling accurate capture of singular heat flux fields at the fiber center that are challenging for conventional approaches. In contrast, continuity and periodicity conditions are enforced via boundary collocation points in the loss function. Validation against finite element simulations across a wide range of fiber volume fractions shows that accurate and converged temperature distributions can be achieved after 9000 training epochs using 8-16 harmonic terms. Additional higher-order harmonics are difficult to train reliably and may degrade predictions. While strong agreement is observed in the matrix heat flux distributions, noticeable discrepancies persist in the fiber phase due to varying

ability to capture the singular heat flux fields. Furthermore, uniform collocation points converge faster than random points during solution refinement. Finally, transfer learning is employed to accelerate training for new configurations, allowing the network to achieve comparable accuracy after only 2000 training epochs, which is substantially fewer than the 9,000 epochs required when training from scratch.

Keywords: Physics-informed neural networks; Micromechanics; Graphite fiber; Composites; Elasticity

1 Introduction

Graphite/carbon fiber-reinforced composites are extensively used in aerospace, automotive, wind energy, and sports equipment due to their high strength-to-weight ratio, excellent fatigue resistance, and favorable thermal properties [1]. For simplicity, graphite fibers are often treated as transversely isotropic material; however, their actual behavior can range from transverse isotropy to cylindrical orthotropy, depending on the alignment of graphite basal planes around the fiber axis [2]. As illustrated in Figure 1(a), for transversely isotropic (TI) fiber, there is no preferred alignment of basal planes, leading to a randomly distributed graphitic microstructure in the cross-sectional plane. For radially orthotropic fiber (RO) (Figure 1b), the stiff basal planes are predominantly aligned in the radial direction with concomitant microstructure resembling a bicycle wheel, while the circumferentially orthotropic (CO) fiber (Figure 1c) has its stiff basal planes primarily oriented in the circumferential direction, producing onion-like microstructures. In composites reinforced with these types of fibers, variations in the underlying morphological microstructures can lead to markedly different local

temperature and heat flux field distributions, even if the overall homogenized thermal conductivities remain similar. At higher fiber volume fractions, the influence of fiber morphology becomes more pronounced, affecting both the local fields and the effective composite response. Therefore, accurately accounting for these morphological effects is crucial for reliable prediction of the thermo-mechanical behavior of graphite fiber-reinforced composites under complex loading and environmental conditions.

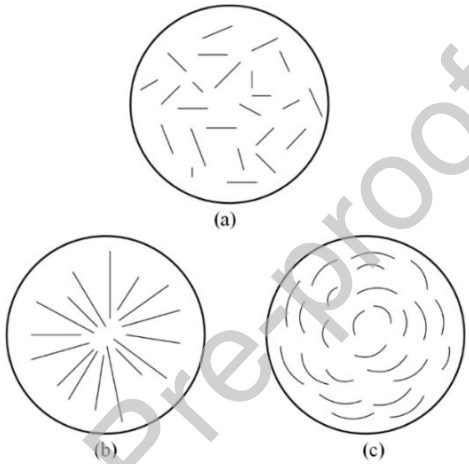

Figure 1 Graphite fibers with different underlying morphological microstructures: (a) transversely isotropic (TI); (b) radially orthotropic (RO); (c) circumferentially orthotropic (CO)

Thus far, various analytical and numerical models have been developed by several investigators to quantify the impacts of the fiber orthotropy on the local stress and temperature field variable distributions and, hence, the homogenized behaviors of the composite media. In the early work of Avery and Herakovich [3], an elasticity solution was developed for a composite cylinder geometry model to study the effect of graphite fiber orthotropy on the fabrication-induced residual stresses and the resulting damage mechanisms. Subsequently, Hashin [4] provided solutions based on the well-known composites cylinder assemblage model (CCA) for homogenized moduli of unidirectional graphite/epoxy composites and related stress fields. Chen et al. [5]

developed the Mori-Tanaka method to identify the local stress fields and effective thermoelastic properties of coated fiber composites with cylindrically orthotropic fibers. In these contributions, the cylindrically orthotropic graphite fiber was replaced by its transversely isotropic equivalence, eliminating the consideration of the detailed angular dependence of the elastic moduli of the graphite fiber in the micromechanics formulation. Extension of these models to explicitly account for the cylindrically orthotropic phases is not straightforward and has only been successful by Chatzigeorgiou et al. [6] and Chen et al. [7], who employed the CCA and Mori-Tanaka models, respectively, along with the transformation analysis technique (TFA) to calculate the inelastic response of unidirectional graphite/epoxy composites with radially orthotropic coating layers. While the above idealized geometric models can provide reasonable estimates of the homogenized moduli, they are insufficient for capturing the detailed local stress and heat flux field distributions within the constituent phases. This limitation is particularly evident in reproducing the singular stress and heat flux fields in radially or circumferentially orthotropic fibers, which are critical for accurate local damage predictions.

The locally exact homogenization theory (LEHT) developed by Wang and Pindera [8] and Wang et al. [9] was perhaps the first to explicitly take into account the morphological effect of graphite fiber in a repeating unit cell (RUC) representing the composite's microstructure. The LEHT enables the rapid and accurate identification of homogenized moduli and concomitant local temperature and stresses in unidirectional composites with cylindrically orthotropic phases. The success of the theory lies in the

accurate imposition of periodicity conditions along the boundaries of hexagonal and square repeating microstructures via a balanced variational principle, cf. Drago and Pindera [10]. The latter provides converged coefficients in the series expansion of temperature and displacement fields that satisfy stress equilibrium governing differential equations, as well as the interfacial continuity and periodicity conditions. Alternative approach to the LEHT is the recently proposed isogeometric homogenization technique (IGH) by Du et al. [11], for unidirectional composites reinforced with cylindrically orthotropic fibers. In contrast to the classical finite element approach, the IGH theory utilizes Nitsche's method to simultaneously enforce interfacial traction and displacement continuity, along with periodic boundary conditions, an essential step for capturing the smooth stress fields characteristic of this class of materials. However, just like the classical FEM approaches, the IGH technique suffers from accuracy issues in the presence of singularities, where the smooth basis functions used in the isogeometric framework are not very effective in capturing localized stress concentrations.

Recent advances in computational capabilities have renewed interest in neural network-based approaches for solving partial differential equations (PDEs) with given spatio-temporal boundary conditions. A key development in this area is the physics-informed neural network (PINN), developed by Raissi et al. [12], which integrates the strong-form PDEs and boundary conditions directly into the loss function formulation by automatic differentiation. Since the introduction of PINN [12], numerous variants have been formulated. For instance, Saidaoui et al. [13] proposed the deep NURBS

method, which provides accurate and computationally efficient solutions for PDEs on arbitrary geometries, while rigorously enforcing Dirichlet boundary conditions. Yu et al. [14] introduced the gradient-enhanced PINN for improving the accuracy of the PINN. Within the framework of continuum mechanics, Haghighat et al. [15] proposed a PINN model to model elastic and elastoplastic solid mechanics problems, demonstrating their effectiveness in both forward simulations and inverse parameter identification. Samaniego et al. [16] developed the deep energy approach, in which the total potential energy is formulated as the loss function. Thorough reviews of various techniques in embedding physics into machine learning are provided by Karniadakis et al. [17] and Toscano et al. [18].

The PINN has been utilized to predict the local stress fields in composites with various degrees of success. For instance, Henkes et al. [19] applied PINNs to model the nonlinear stress and displacement fields arising from material inhomogeneities with sharp phase interfaces. Ren and Lyu [20] developed the mixed form-based physics-informed neural networks for performance evaluation of two-phase random materials. Guo et al. [21] proposed a deep collocation method incorporating transfer learning to solve potential problems in non-homogeneous media, enhancing both generality and robustness. Wu et al. [22] employed PINN to identify heterogeneous micromechanical properties of biological tissues. A common limitation of the above work is that the periodic boundary conditions, which are essential in micromechanics theory, are not exactly satisfied. To address the issue, Jiang et al. [23] proposed the deep homogenization neural network method for predicting temperature and heat flux fields

in composites, where the network architecture inherently enforces periodic boundary conditions. Wu et al. [24] extended the approach to identify local stress distributions and homogenized moduli in heterogeneous periodic arrays with two- or three-dimensional microstructures under general macroscopic loading conditions. Linghu et al. [25] proposed a higher-order multiscale neural network approach for studying the quasi-static thermo-mechanical problems of composite materials. However, deep neural networks face significant challenges when the solution field exhibits sharp variations. As a result, the conventional PINN cannot be utilized to predict the singular stress and heat flux field commonly observed in the cylindrically orthotropic fibers [26, 27].

The elasticity-inspired data-driven micromechanics model developed by Chen et al. [28] provides an easy-to-implement framework for the micromechanics analysis of periodic microstructures. In this approach, the displacements in the fiber and matrix domains are represented using discrete Fourier expansions using two custom-tailored network models derived from the solutions of Navier's displacement equations. The coefficients of these discrete Fourier expansions of the displacements are directly obtained by minimizing the displacement and traction losses associated with interfacial continuity and periodicity conditions, avoiding the complex implementation of both traction and displacement periodicity boundary conditions through the balanced variational principle. An additional advantage of the neural network-based homogenization lies in the fact that the partial derivatives of the displacements are computed via automatic differentiation with minimal human input. A researcher

untrained in the techniques of homogenization would be able to obtain the homogenized and local response of periodic composites by using this algorithm.

Herein, we present a new micromechanics-informed neural network model for identifying the local temperature and heat flux in periodic unidirectional thermoconductive composites with cylindrically isotropic phases. Dual neural networks are used to predict the temperature fields in the matrix and fiber phases of composites, formulated explicitly using discrete Fourier expansions. In addition, to facilitate the implementation of periodic boundary conditions, the temperature field in the matrix is represented using a two-scale expansion involving the macroscopic and microscopic contributions. In contrast, the temperature field in the fiber is directly expressed in the local coordinate in order to correctly capture the singular stress field in cylindrically orthotropic fibers. This framework produces rapid convergence of the local temperature and heat flux fields upon the satisfaction of the continuity and periodicity conditions of temperature and heat flux enforced through a set of material points. The main contributions of the present work include:

- Development of micromechanics-informed neural network for homogenization of periodic microstructures with cylindrically orthotropic phases.
- Integration of elasticity solutions directly into the neural network architecture to accurately capture singular heat flux fields.
- Application of transfer learning to efficiently train the model on new geometries using knowledge from pre-trained microstructures.

It should be noted that the present framework can be regarded as a specific

implementation of PINN. The key distinction lies in how the governing PDE and boundary conditions are enforced. In this work, the PDE is hard-imposed, enabling accurate capture of the singular heat flux at the fiber center, which is notoriously challenging for conventional PINN, while the boundary conditions are enforced softly through the loss function. In contrast, conventional PINN applications often hard-impose the boundary conditions [13], with the PDE relations satisfied in a soft manner.

2 Theoretical developments

Without loss of generality, let us consider hexagonal or square arrays of unidirectional orthotropic fibers in an orthotropic matrix. As shown in Figure 2, the responses of such composites can be characterized by a repeating unit cell (RUC), namely, the smallest basic building block, subjected to periodic boundary conditions [29], with the fiber assumed to be positioned in the unit cell center for simplicity. Following the asymptotic homogenization theory [30], the temperature $T^{(m)}$ field in the matrix phase of the composite can be expressed in terms of two-scale expansion involving the macroscopic $\bar{T}(\mathbf{x})$ and fluctuating $T'^{(m)}(\mathbf{y})$ contributions in the global Cartesian and local cylindrical coordinates, respectively, as follows:

$$T^{(m)}(\mathbf{x},\mathbf{y}) = \bar{T}(\mathbf{x}) + T'^{(m)}(\mathbf{y}) \tag{1}$$

where $\bar{T}(\mathbf{x}) = \bar{H}_i x_i$, and $\bar{H}_i$ indicates the averaged (or applied) temperature gradient. $\mathbf{x} = [x_1, x_2, x_3]$, $\mathbf{y} = [r, \theta]$. The superscript (m) indicates the matrix phase. The above temperature generates local temperature gradients in the following form:

$$H_1^{(m)} = \bar{H}_1, \quad H_r^{(m)} = \bar{H}_r + \frac{\partial T'^{(m)}}{\partial r}, \quad H_\theta^{(m)} = \bar{H}_\theta + \frac{1}{r}\frac{\partial T'^{(m)}}{\partial \theta} \tag{2}$$

It is noted that the above temperature field decomposition is essential for the implementation of the periodicity boundary conditions in the matrix phase. However, for cylindrically orthotropic fibers exhibiting singular or vanishing heat flux at the fiber origin, depending on the type of orthotropy, this two-scale decomposition is no longer suitable [8]. Hence, the fiber temperature field is represented strictly in terms of local unit cell coordinates $T^{(f)}\left(x_1, r, \theta\right)$. Accordingly, the local temperature gradients in the fiber phase read:

$$H_1^{(f)} = \bar{H}_1, \quad H_r^{(f)} = \frac{\partial T^{(f)}}{\partial r}, \quad H_\theta^{(f)} = \frac{1}{r}\frac{\partial T^{(f)}}{\partial \theta} \tag{3}$$

where the superscript (f) indicates the fiber phase.

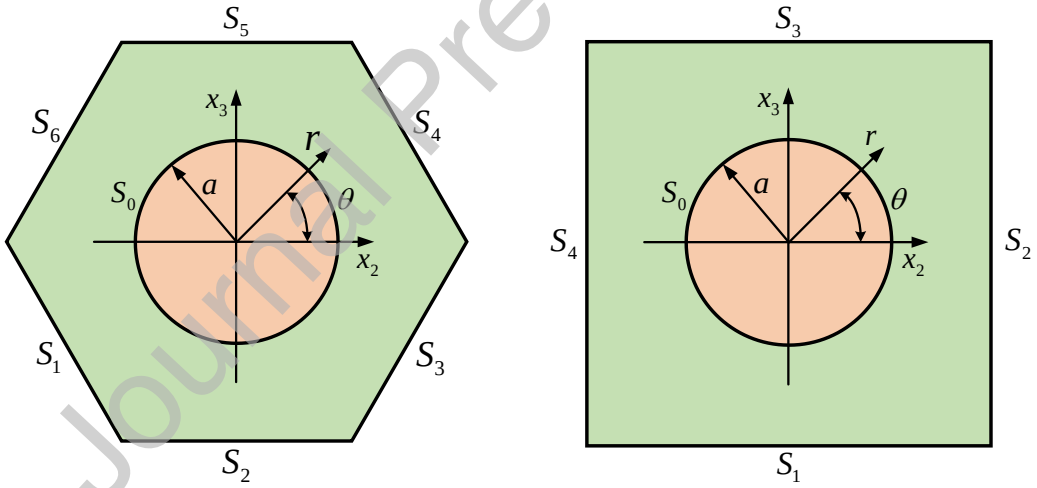

Figure 2 Repeating unit cell with cylindrical fibers:(a) hexagonal array; (b) square array

The local temperature field $T^{(p)}$ in the pth phase of the composites is determined by satisfying the continuity condition and periodicity condition, as well as the local steady state heat condition governing equation as follows:

$$\frac{\partial q_1^{(p)}}{\partial x_1} + \frac{\partial q_r^{(p)}}{\partial r} + \frac{1}{r}\frac{\partial q_\theta^{(p)}}{\partial \theta} = 0 \tag{4}$$

where $p = f, m$, $q_i^{(p)}$ indicates the heat flux. For a cylindrically orthotropic solid, the Fourier's law that relates the heat flux to the temperature gradient can be expressed as:

$$\begin{bmatrix} q_1 \\ q_r \\ q_\theta \end{bmatrix}^{(p)} = -\begin{bmatrix} k_A & 0 & 0 \\ 0 & k_r & 0 \\ 0 & 0 & k_\theta \end{bmatrix}^{(p)} \begin{bmatrix} H_1 \\ H_r \\ H_\theta \end{bmatrix}^{(p)} \tag{5}$$

where k_A, k_r and k_θ denote the coefficients of thermo-conductivity in axial, radial, and tangent directions, respectively. It should be noted that for RO fiber, the ratio $k_r/k_\theta > 1$, while for CO fiber, the ratio $k_r/k_\theta < 1$. For TI fiber, $k_r/k_\theta = 1$.

Substituting the temperature-gradient relation, Eq. (2), into Fourier's law, Eq. (5), and subsequently into the heat flux governing equation, Eq. (4), we obtain the governing equation for steady-state heat conduction expressed in terms of the temperature field [31]:

$$\frac{\partial^2 T^{(p)}}{\partial r^2} + \frac{1}{r}\frac{\partial T^{(p)}}{\partial r} + \frac{k_\theta}{k_r}\frac{1}{r^2}\frac{\partial^2 T^{(p)}}{\partial \theta^2} = 0 \tag{6}$$

The solution for the temperature field $T^{(p)}\left(p = f, m\right)$ in Eq. (6) has the following form:

$$T^{(f)}\left(x_1, r, \theta\right) = \bar{H}_1 x_1 + \sum_{n=0}^{\infty}\left[h_n^{(f)}(r)\cos n\theta + h_n^{*(f)}(r)\sin n\theta\right] \tag{7}$$

$$T^{(m)}\left(\mathbf{x}, r, \theta\right) = \bar{H}_i x_i + \sum_{n=0}^{\infty}\left[h_n^{(m)}(r)\cos n\theta + h_n^{*(m)}(r)\sin n\theta\right] \tag{8}$$

where $h_n^{(f,m)}(r)$ and $h_n^{*(f,m)}(r)$ are the unknown functions from the Fourier transform.

Substituting Eqs. (7) and (8) into Eq. (6), we obtain

$$T^{(f)}\left(x_1, r, \theta\right) = \bar{H}_1 x_1 + \sum_{n=1}^{\infty} a\left[\left(\zeta^{\lambda_n^f} F_{n1}^f + \zeta^{-\lambda_n^f} F_{n3}^f\right)\cos n\theta + \left(\zeta^{\lambda_n^f} F_{n2}^f + \zeta^{-\lambda_n^f} F_{n4}^f\right)\sin n\theta\right] \tag{9}$$

$$T^{(m)}(\mathbf{x},r,\theta)=\bar{H}_i x_i+\sum_{n=1}^{\infty}a\left[\left(\zeta^n F_{n1}^m+\zeta^{-n}F_{n3}^m\right)\cos n\theta+\left(\zeta^n F_{n2}^m+\zeta^{-n}F_{n4}^m\right)\sin n\theta\right] \quad (10)$$

where $\zeta=r/a$ denotes the normalized radial coordinate with regard to the fiber radius a. $\lambda_n^f=n\sqrt{k_\theta/k_r}$ denotes the eigenvalue. $F_{nj}^{f,m}\left(j=1,2,3,4\right)$ denotes the unknown coefficients determined from the continuity and periodicity conditions. We note that $F_{n3}^f=F_{n4}^f=0$ to ensure that the temperature remains a finite value at the fiber center ($r=0$).

It is assumed that periodic boundary conditions are valid since the material microstructure is periodic and there is a clear separation between the micro- and macro-scales [32]. The coefficients $F_{nj}^{f,m}\left(j=1,2,3,4\right)$ are the fundamental unknowns that need to be determined through the enforcement of the interfacial continuity condition at the fiber/matrix interface and the periodicity condition at the opposing faces of the hexagonal and square RUCs, for both temperature and heat flux, as follows:

1) Interfacial continuity condition:

$$\begin{aligned}&T^{(f)}\left(S_0\right)=T^{(m)}\left(S_0\right),\\&q_n^{(f)}\left(S_0\right)+q_n^{(m)}\left(S_0\right)=0\end{aligned} \quad (11)$$

2) Periodicity condition:

for hexagonal arrays,

$$\begin{aligned}&T'^{(m)}\left(S_1\right)=T'^{(m)}\left(S_4\right),\\&T'^{(m)}\left(S_2\right)=T'^{(m)}\left(S_5\right),\\&T'^{(m)}\left(S_3\right)=T'^{(m)}\left(S_6\right),\\&q_n^{(m)}\left(S_1\right)+q_n^{(m)}\left(S_4\right)=0,\\&q_n^{(m)}\left(S_2\right)+q_n^{(m)}\left(S_5\right)=0,\\&q_n^{(m)}\left(S_3\right)+q_n^{(m)}\left(S_6\right)=0\end{aligned} \quad (12)$$

for square arrays,

$$\begin{aligned} T'^{(m)}\left(S_1\right) &= T'^{(m)}\left(S_3\right), \\ T'^{(m)}\left(S_2\right) &= T'^{(m)}\left(S_4\right), \\ q_n^{(m)}\left(S_1\right) + q_n^{(m)}\left(S_3\right) &= 0, \\ q_n^{(m)}\left(S_2\right) + q_n^{(m)}\left(S_4\right) &= 0 \end{aligned} \tag{13}$$

In the above equation, $q_n = q_i n_i$ denotes heat flux normal to the $S_{(.)}$ face, and n_i denotes the component of the outward unit normal vector. It should be noted that, although the governing differential equations for heat conduction are exactly satisfied for each harmonic representation, the unit cell problem is solved approximately in practice, as only a limited number of harmonic terms can be retained, resulting in the periodicity and continuity boundary conditions not being strictly satisfied.

3 Micromechanics-informed neural networks

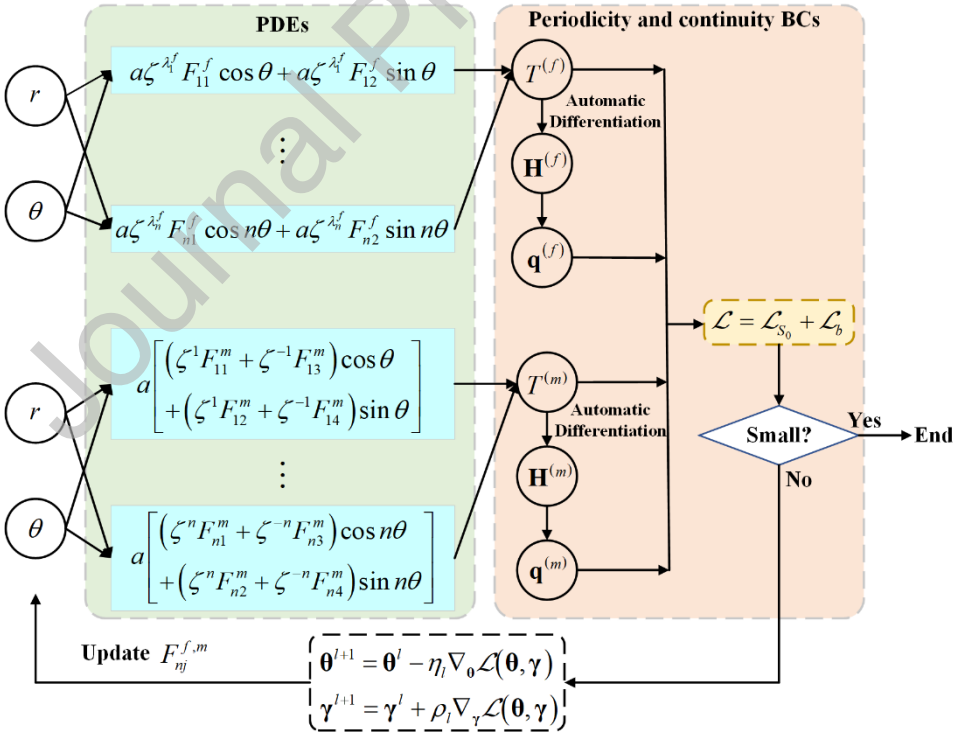

Figure 3 Architecture of the proposed micromechanics-informed neural networks

As shown in Figure 3, we employ distinct neural networks (NN) to represent the

temperature fields in each phase of the composites, as follows:

$$T^{(f)}\left(x_1, r, \theta\right) = \bar{H}_1 x_1 + NN^{(f)}\left[r, \theta\right] \tag{14}$$

$$T^{(m)}\left(\mathbf{x}, r, \theta\right) = \bar{H}_i x_i + NN^{(m)}\left[r, \theta\right] \tag{15}$$

namely, a mapping from $\mathbb{R}^2 \to \mathbb{R}^1$. In the above equation, $x_2 = r\cos\theta$, $x_3 = r\sin\theta$. The solutions for the fiber and matrix temperature fields are hardcoded in the network architectures, with the coefficients of each harmonic term $F_{nj}^{f,m}\left(j = 1,2,3,4\right)$ treated as trainable parameters. Under macroscopic temperature gradients $\bar{\mathbf{H}} = \left[\bar{H}_1, \bar{H}_2, \bar{H}_3\right]^{\mathrm{T}}$, these parameters are optimized by minimizing a cost function, in which the boundary $\mathcal{L}_b$ and interface $\mathcal{L}_{S_0}$ losses are softly constrained to enforce the continuity and periodicity of both the temperature field and the heat fluxes:

$$\text{ArgMin}: \mathcal{L} = \mathcal{L}_{S_0} + \mathcal{L}_b \tag{16}$$

In the above equation:

$$\mathcal{L}_{S_0} = \frac{1}{N_0}\sum_{k=1}^{k=N_0} \gamma_0^k \left[\left(q_n^{(f)}\left(S_{0k}\right) + q_n^{(m)}\left(S_{0k}\right)\right)^2 + \left(T^{(f)}\left(S_{0k}\right) - T^{(m)}\left(S_{0k}\right)\right)^2\right] \tag{17}$$

for the hexagonal arrays $\mathcal{L}_b = \mathcal{L}_{S_1-S_4} + \mathcal{L}_{S_2-S_5} + \mathcal{L}_{S_3-S_6}$ with:

$$\mathcal{L}_{S_1-S_4} = \frac{1}{N}\sum_{k=1}^{k=N} \gamma_1^k \left[\left(q_n^{(m)}\left(S_{1k}\right) + q_n^{(m)}\left(S_{4k}\right)\right)^2 + \left(T'^{(m)}\left(S_{1k}\right) - T'^{(m)}\left(S_{4k}\right)\right)^2\right] \tag{18}$$

$$\mathcal{L}_{S_2-S_5} = \frac{1}{N}\sum_{k=1}^{k=N} \gamma_2^k \left[\left(q_n^{(m)}\left(S_{2k}\right) + q_n^{(m)}\left(S_{5k}\right)\right)^2 + \left(T'^{(m)}\left(S_{2k}\right) - T'^{(m)}\left(S_{5k}\right)\right)^2\right] \tag{19}$$

$$\mathcal{L}_{S_3-S_6} = \frac{1}{N}\sum_{k=1}^{k=N} \gamma_3^k \left[\left(q_n^{(m)}\left(S_{3k}\right) + q_n^{(m)}\left(S_{6k}\right)\right)^2 + \left(T'^{(m)}\left(S_{3k}\right) - T'^{(m)}\left(S_{6k}\right)\right)^2\right] \tag{20}$$

for square arrays $\mathcal{L}_b = \mathcal{L}_{S_1-S_3} + \mathcal{L}_{S_2-S_4}$ with:

$$\mathcal{L}_{S_1-S_3}=\frac{1}{N}\sum_{k=1}^{k=N}\gamma_1^k\left[\left(q_n^{(m)}\left(S_{1k}\right)+q_n^{(m)}\left(S_{3k}\right)\right)^2+\left(T'^{(m)}\left(S_{1k}\right)-T'^{(m)}\left(S_{3k}\right)\right)^2\right] \tag{21}$$

$$\mathcal{L}_{S_2-S_4}=\frac{1}{N}\sum_{k=1}^{k=N}\gamma_2^k\left[\left(q_n^{(m)}\left(S_{2k}\right)+q_n^{(m)}\left(S_{4k}\right)\right)^2+\left(T'^{(m)}\left(S_{2k}\right)-T'^{(m)}\left(S_{4k}\right)\right)^2\right] \tag{22}$$

In the above equations, S_{ik} denotes the kth collocation points on the S_i face. N_0 and N denotes the total number of collocation points on the fiber/matrix interface S_0 and the S_i face, respectively. γ_i^k are adjustable trainable weights associated with kth collocation point on the ith face in each heat flux and temperature loss term, respectively. It should be emphasized that the temperature gradients in Eqs. (2) and (3) necessary for the evaluation of the heat flux can be directly computed using automatic differentiation in the PyTorch library, and have been numerically verified by the authors to match the analytical results.

During the training of the network model, to obtain harmonic eigenfunction coefficients $\boldsymbol{\theta}$ under arbitrary macroscopic temperature gradients $\bar{\mathbf{H}}$, and consequently the local temperature fields, we attempt to minimize the total loss function $\mathcal{L}$ with regard to the harmonic eigenfunction coefficients $\boldsymbol{\theta}=\left[F_{n1}^{(m)},F_{n2}^{(m)},F_{n3}^{(m)},F_{n4}^{(m)},F_{n1}^{(f)},F_{n2}^{(f)}\right]$ based on the gradient descent, but concurrently maximize the total loss function about the adaptive weights $\boldsymbol{\gamma}$ based on the gradient ascent as follows [33]:

$$\begin{aligned}\boldsymbol{\theta}^{l+1}&=\boldsymbol{\theta}^{l}-\eta_l\nabla_{\boldsymbol{\theta}}\mathcal{L}\left(\boldsymbol{\theta},\boldsymbol{\gamma}\right),\\ \boldsymbol{\gamma}^{l+1}&=\boldsymbol{\gamma}^{l}+\rho_l\nabla_{\boldsymbol{\gamma}}\mathcal{L}\left(\boldsymbol{\theta},\boldsymbol{\gamma}\right)\end{aligned} \tag{23}$$

where l indicates the lth training epoch. η_l and ρ_l indicate the non-negative learning rates for the harmonic eigenfunction coefficients and adaptive weights $\boldsymbol{\gamma}$,

respectively. The rationale is that the weights assigned to collocation points increase with their corresponding losses. As a result, collocation points associated with larger errors are automatically given greater emphasis in the total loss function during its minimization. This ensures that the training process focuses more on regions where the solution is less accurate [34].

4. Numerical results

4.1 Convergence study

We first demonstrate the developed theory's convergence behavior by calculating the local temperature and heat flux distributions as a function of harmonic eigenfunctions in the temperature field representation. The investigated microstructure consists of the unidirectional graphite/epoxy composites. The thermal conductivities of the graphite fiber and the polymer matrix, taken directly from Wang et al. [9], are listed in Table 1 for the reader's convenience.

Table 1 Thermal conductivities for graphite fiber and polymer matrix

	$k_r\left(\mathrm{W\cdot m^{-1}\cdot K^{-1}}\right)$	$k_\theta\left(\mathrm{W\cdot m^{-1}\cdot K^{-1}}\right)$	$k_A\left(\mathrm{W\cdot m^{-1}\cdot K^{-1}}\right)$
RO fiber	7.0	2.9	7.0
CO fiber	2.9	7.0	7.0
TI fiber	4.5	4.5	7.0
Polymer	0.5	0.5	0.5

Hexagonal and square unit cells with 60% fiber volume fraction were utilized in this convergence study. The significant fiber-fiber interactions at such a high-volume fraction make it an excellent benchmark for evaluating the model's accuracy. Circumferentially orthotropic fibers were employed for the calculation of temperature and heat flux fields. Figure 4 depicts the collocation point distributions along each face

of the unit cell. 200 collocation points were distributed uniformly on each exterior face of the unit cell, as well as along the fiber/matrix interface. A transverse macroscopic temperature gradient $\bar{H}_2 = 1\mathrm{K/m}$ was applied.

Figure 5 demonstrates the variation of total loss residuals as a function of training epochs for the hexagonal and square unit cell architectures under different numbers of harmonic eigenfunctions. It is noted that the neural networks were trained using the Adam optimizer in PyTorch with an initial learning rate of 0.01. To prevent the oscillation of the loss function caused by excessive updates of the harmonic coefficients during solution refinement, this rate was held constant for the first 7000 epochs and then reduced by a factor of 0.5 for every 1000 epochs. Training was terminated at 12000 epochs, as the loss values had stabilized after 9000 epochs. As shown, increasing the number of harmonic terms generally reduces the minimal loss value. In practice, however, incorporating more terms complicates training, since the small higher-order coefficients are more difficult for the network to learn accurately. In fact, the loss values increase substantially when 20 harmonics are used for the hexagonal unit cell and 16 for the square unit cell.

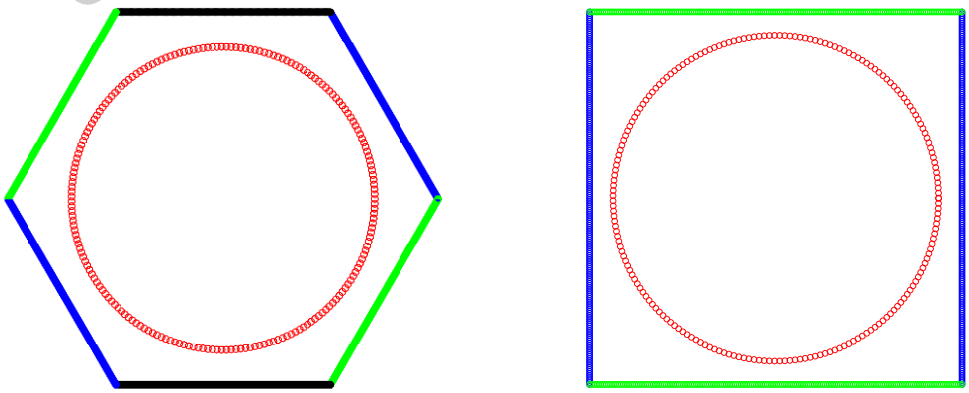

(a) (b)

Figure 4 Collocation point distributions in the faces of (a) hexagonal unit cell; (b) square unit cell

with 60% volume fraction. It is noted that on the exterior faces, the collocation points are distributed periodically to enforce the periodic boundary conditions

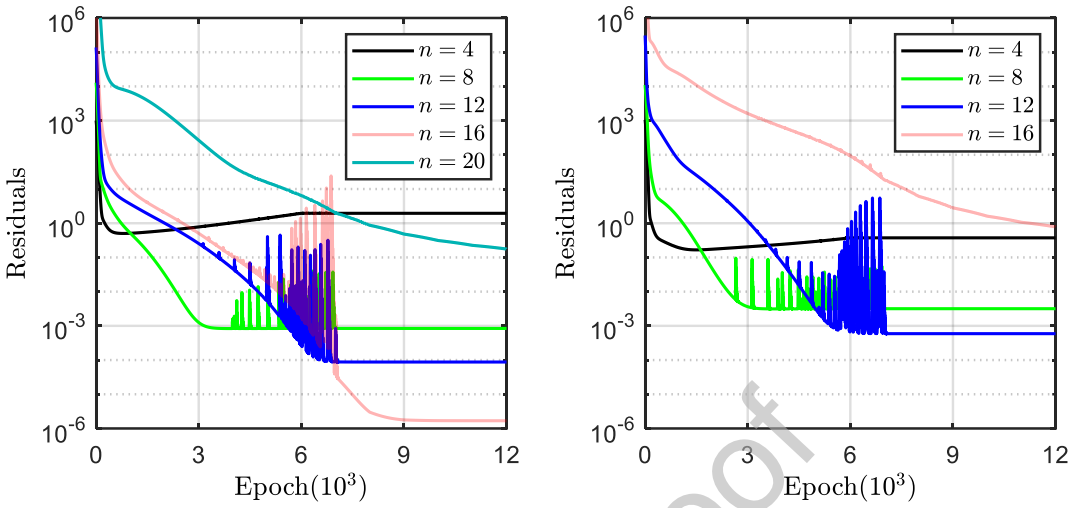

Figure 5 Comparison of the neural network training loss as a function of harmonic eigenfunction number for (a) hexagonal unit cell; (b) square unit cell

Figures 6 and 7 compare the fluctuating temperature fields in the hexagonal and square unit cells, respectively, predicted by the trained neural networks for different numbers of harmonic eigenfunctions. Using only four harmonic eigenfunctions fails to accurately reproduce the temperature distributions. In contrast, employing 8, 12, or 16 harmonic eigenfunctions in the hexagonal unit cell, and 8 or 12 in the square unit cell, produces virtually identical results. While it is true that including higher-order terms should, in principle, improve the accuracy of the NN solution, the magnitudes of the harmonic coefficients span several orders of magnitude, as shown in Table 3 in the sequel. This large disparity makes it difficult for the network to accurately learn all harmonic coefficients, particularly the smaller ones. Therefore, further increasing the number of harmonic eigenfunctions to 20 for the hexagonal unit cell and to 16 for the square unit cell deteriorates the predictions, since the NN struggles to learn the higher-

order coefficients and introduces spurious fluctuations.

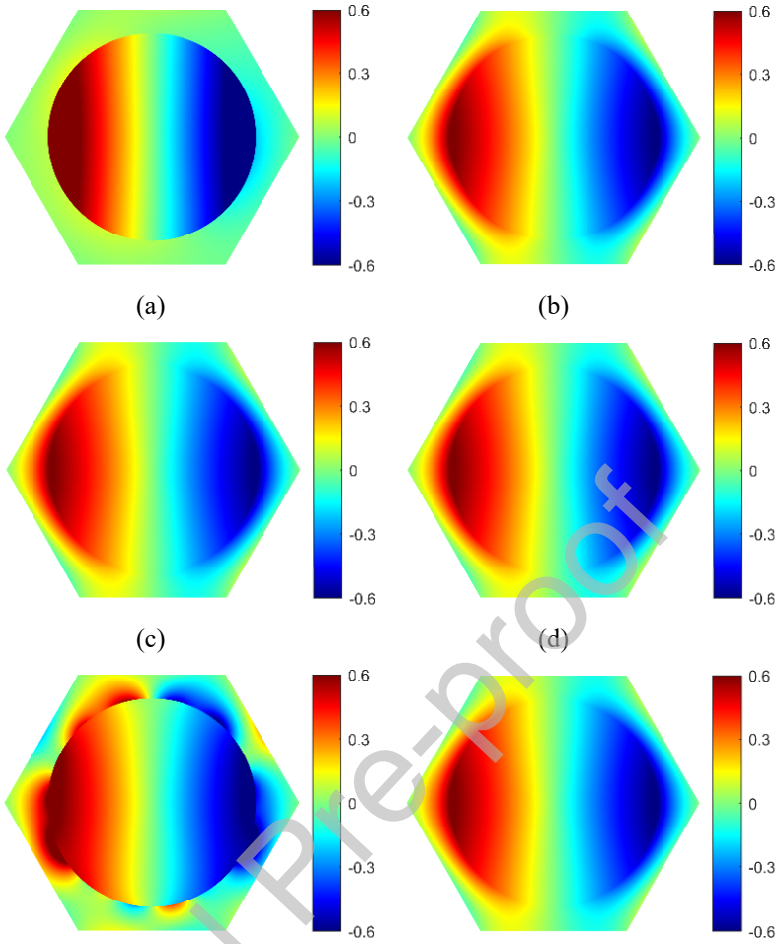

Figure 6 Comparison of fluctuating temperature $T'(\mathrm{K})$ distributions in hexagonal arrays of CO fiber: (a) NN with $n=4$; (b) NN with $n=8$; (c) NN with $n=12$; (d) NN with $n=16$; (e) NN with $n=20$; (f) FEM

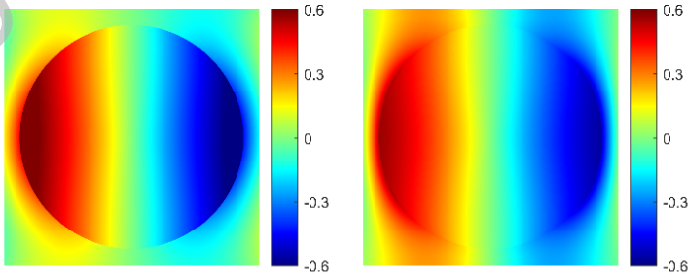

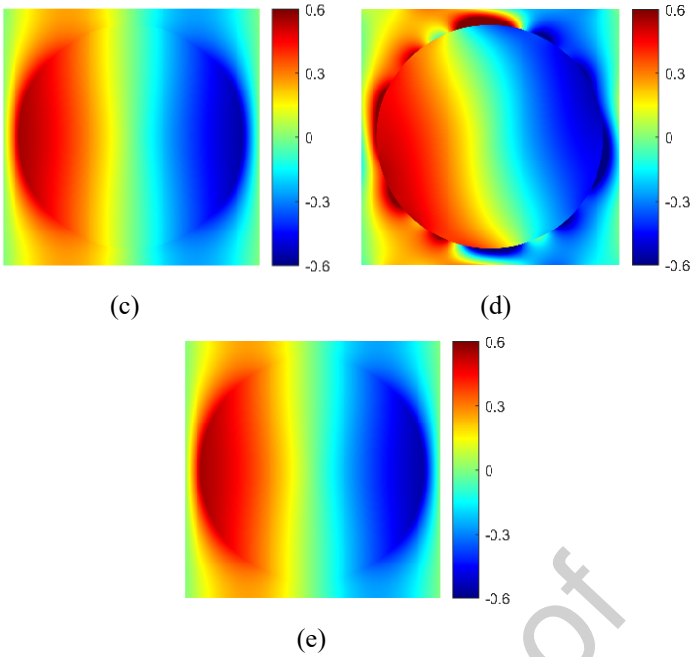

Figure 7 Comparison of fluctuating temperature $T'(\mathrm{K})$ distributions in square arrays of CO fiber: (a) NN with $n=4$; (b) NN with $n=8$; (c) NN with $n=12$; (d) NN with $n=16$; (e) FEM

Table 2 compares the training time of the proposed NN approach up to 9000 epochs, when the loss reached its minimum, with the execution time of the FEM. The NN was implemented using the PyTorch library, while the FEM was computed with an in-house MATLAB code. All computations were performed on a Windows PC with a 13th Gen Intel® Core™ i9-13900H CPU, 32 GB RAM, and an NVIDIA® RTX 4070 GPU with 24 GB memory. It is observed that the NN approach requires significantly longer execution times than FEM simulations, as the unit cell problem is reformulated as an optimization task, with gradient-based optimization being inherently expensive. Moreover, square unit cells exhibit shorter execution times compared to hexagonal ones, since the number of trainable parameters is reduced due to fewer boundary loss terms.

Table 2 Comparison of execution time (in seconds) between the NN and FEM simulations

	$n=8$	$n=12$	$n=16$	FEM
Hexagonal arrays	518	554	561	69
Square arrays	384	390	-	64

Figure 8 presents the point-wise relative error in the fluctuating temperature field between the NN predictions and FEM results for cases where the NN achieves relatively high accuracy. When the number of harmonic terms reaches 12 for both hexagonal and square unit cells, the relative errors become negligible, typically within 2%, in regions where the fluctuating temperature is not near-zero, demonstrating the effectiveness of the proposed neural network approach. The wavy patterns observed in the error plots near the matrix side of the interface are likely caused by truncation of the eigenfunction expansion, which prevents the boundary conditions from being satisfied exactly. As more eigenfunctions are included, these oscillations diminish, and the NN predictions converge more closely toward the FEM benchmark. As further discussed in Section 4.2, the FEM and NN solutions agree well throughout the matrix phase, indicating that the localized oscillations have little impact on the accuracy of the predicted heat flux distributions. From a practical standpoint, such minor discrepancies do not compromise the reliability of the NN approach relative to FEM.

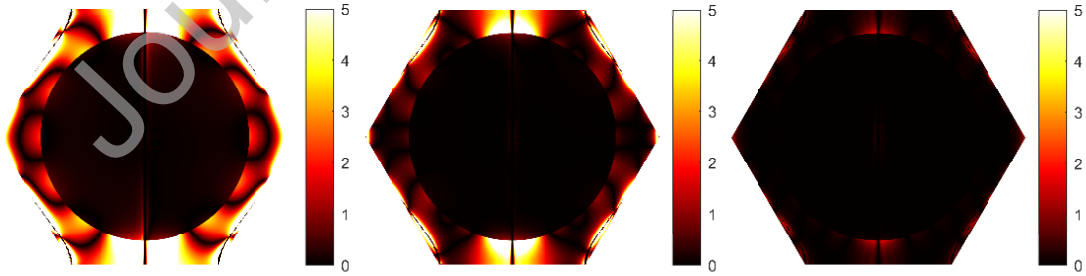

(a) (b) (c)

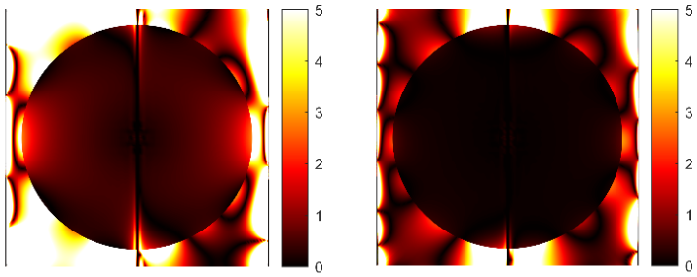

(d) (e)

Figure 8 Comparison of relative percentage error (%) in fluctuating temperature distributions between the FEM and network approach predictions: (a) hexagonal unit cell with $n=8$; (b) hexagonal unit cell with $n=12$; (c) hexagonal unit cell with $n=16$; (d) square unit cell with $n=8$; (e) square unit cell with $n=12$. It is noted that the percentage errors may not be meaningful in regions where the reference temperature is near zero

4.2 Validations

To further examine the modelling and predictive capabilities of the neural network approach for identifying the local temperature and heat flux distributions, we compare the FEM and neural network results for various microstructure configurations. Figures 9-10 show the transverse heat flux q_2 and q_3 distributions in the hexagonal unit cells generated with the FEM and the NN model with 8 and 16 harmonic eigenfunctions, respectively. As observed, the CO fiber produces singular transverse heat flux q_2 at the fiber origin under a transverse macroscopic temperature gradient $\bar{H}_2 = 1\mathrm{K/m}$, while the heat flux q_3 does not. We note that increasing the number of harmonic eigenfunctions in the NN approach from 8 to 16 has little impact on the heat flux distribution in the composites, suggesting that further refinement provides only marginal improvement. Noticeable discrepancies remain between the FEM and NN results in the fiber phase, as the singular heat flux fields are notoriously difficult to capture with the classical FEM. It is well established that FEM inherently loses accuracy near singularities, as it provides only an approximate weak-form solution and does not strictly enforce the local governing differential equations of heat conduction. In contrast, the NN formulation directly enforces the governing equations, enabling a more faithful representation of singular heat flux fields at the fiber center. In addition, a closer examination of the fiber heat flux distributions obtained from the FEM reveals

that they are not continuous across different elements (indicated by the white lines in Figure 9a). This occurs because the classical FEM homogenization technique satisfies only the C^0 continuity of temperature. In contrast, the NN-predicted temperature fields are infinitely differentiable, except at the fiber center where the singularity occurs, resulting in smoothly varying heat flux within each phase. Nonetheless, the NN solution remains approximate because only a limited number of harmonic terms can be retained in the NN approach in practice, indicating that the periodicity and continuity boundary conditions are not strictly satisfied. Even so, both FEM and NN successfully reproduce the singular behavior at the fiber center and exhibit strong agreement in the surrounding matrix phase, underscoring the overall reliability of the proposed method.

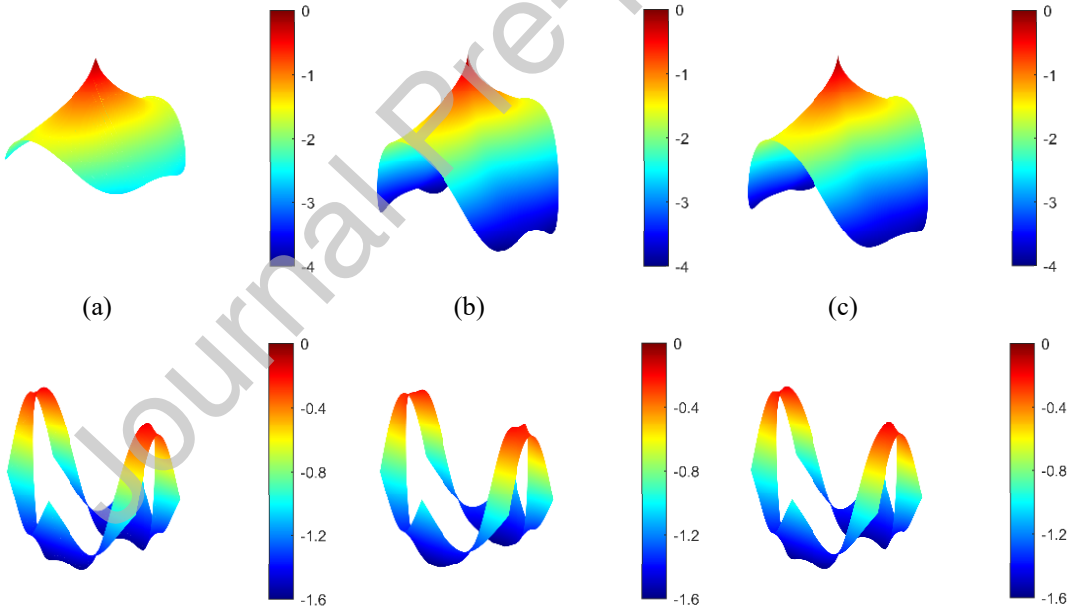

Figure 9 Heat flux $q_2\left(\mathrm{W/m^2}\right)$ distributions in hexagonal array of CO fiber under macroscopic temperature gradient $\bar{H}_2=1\mathrm{K/m}$: (a) fiber heat flux distributions obtained from FEM; (b) fiber heat flux distributions obtained from NN $n=8$; (c) fiber heat flux distributions obtained from NN with $n=16$; (d) matrix heat flux distributions obtained from FEM; (e) matrix heat flux distributions obtained from NN $n=8$; (f) matrix heat flux distributions obtained from NN with $n=16$

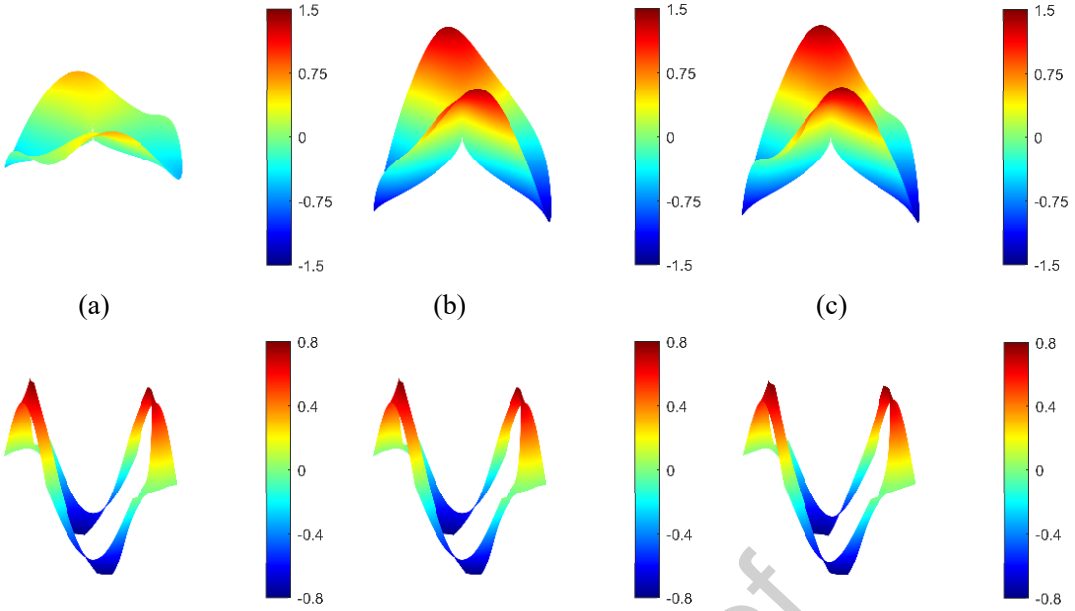

Figure 10 Heat flux $q_3\left(\mathrm{W/m^2}\right)$ distributions in hexagonal array of CO fiber under macroscopic temperature gradient $\bar{H}_2=1\mathrm{K/m}$: (a) fiber heat flux distributions obtained from FEM; (b) fiber heat flux distributions obtained from NN $n=8$; (c) fiber heat flux distributions obtained from NN with $n=16$; (d) matrix heat flux distributions obtained from FEM; (e) matrix heat flux distributions obtained from NN $n=8$; (f) matrix heat flux distributions obtained from NN with $n=16$

Next, we consider a square array of RO fiber with 15% volume fraction. As before, a transverse macroscopic temperature gradient of $\bar{H}_2=1\mathrm{K/m}$ is applied. The small diameter of the fiber relative to the overall unit cell dimensions results in pronounced temperature gradients near the fiber/matrix interface, offering a stringent test of the neural network's robustness. Figure 11 shows the fluctuating temperature distributions and their relative differences generated with the FEM and the NN with 10 harmonic eigenfunctions, demonstrating excellent agreement. Figures 12 and 13 present the corresponding predictions of the transverse heat flux q_2 and q_3 distributions within the unit cell, respectively. It is observed that both the heat flux components q_2 and q_3 exhibit singular behavior at the fiber center. While the FEM and NN predictions of the fiber heat flux distributions show slight differences in magnitude, their predictions for

the matrix heat flux distributions agree closely, further confirming the accuracy of the NN approach. Once again, the FEM predictions of the fiber heat flux distribution show discontinuities across elements due to the limitation of enforcing only C^0 continuity of the temperature fields.

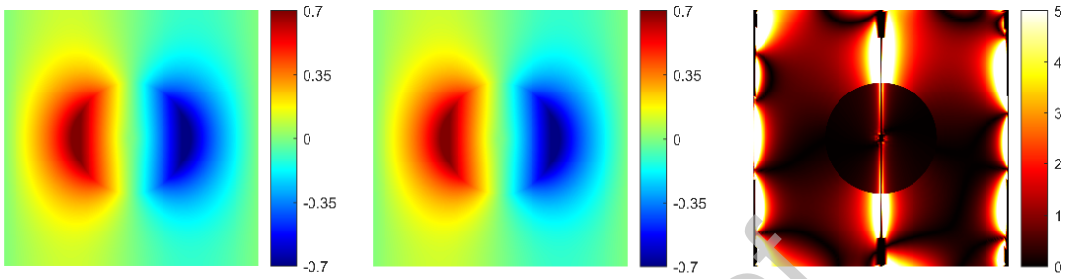

(a) (b) (c)

Figure 11 Fluctuating temperature distributions $T'(\mathrm{K})$ in square array of RO fiber under macroscopic temperature gradient $\bar{H}_2 = 1\mathrm{K/m}$: (a) FEM results; (b) NN results with $n = 10$; (c) relative percentage error (%) between FEM and NN results

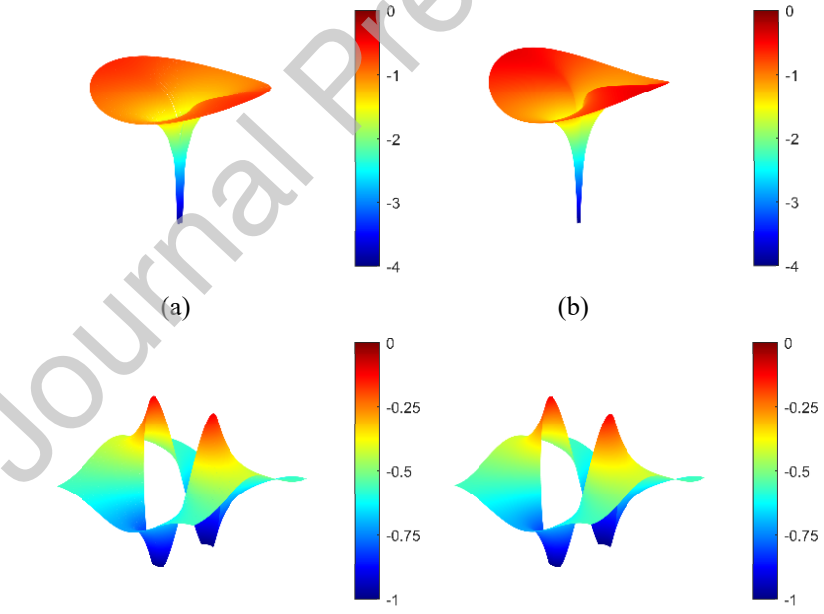

(a) (b)

(c) (d)

Figure 12 Heat flux $q_2\left(\mathrm{W/m^2}\right)$ distributions in square array of RO fiber under macroscopic temperature gradient $\bar{H}_2 = 1\mathrm{K/m}$: (a) fiber heat flux distributions obtained from FEM; (b) fiber flux distributions obtained from NN with $n = 10$; (c) matrix heat flux distributions obtained from FEM; (d) matrix flux distributions obtained from NN with $n = 10$

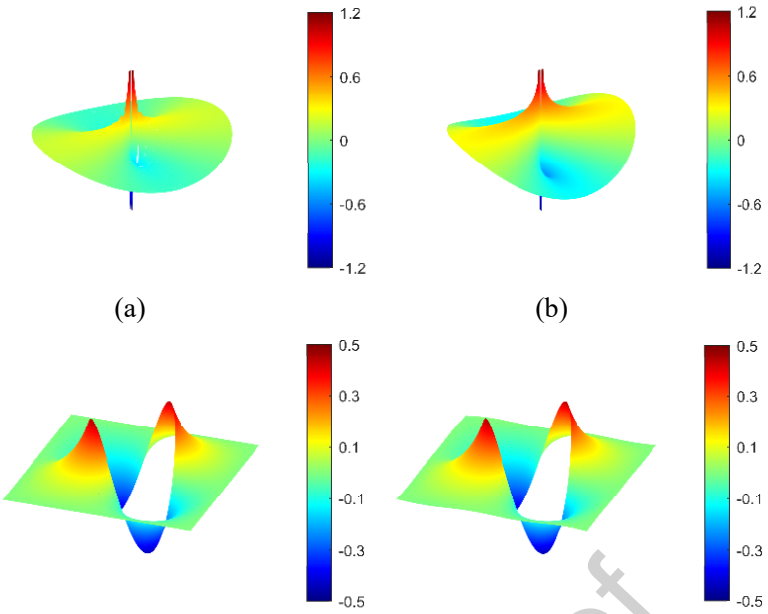

Figure 13 Heat flux $q_3\left(\mathrm{W/m^2}\right)$ distributions in square array of RO fiber under macroscopic temperature gradient $\bar{H}_2=1\mathrm{K/m}$: (a) fiber heat flux distributions obtained from FEM; (b) fiber flux distributions obtained from NN with $n=10$; (c) matrix heat flux distributions obtained from FEM; (d) matrix flux distributions obtained from NN with $n=10$

Figure 14 compares the neural network predicted transverse heat flux distributions for square arrays of RO, CO and TI fibers with 15% fiber content under a transverse macroscopic temperature gradient of $\bar{H}_2=1\mathrm{K/m}$. Unlike cylindrical orthotropic fibers that produce singular heat flux, the TI fiber generates almost uniform distribution, highlighting the importance of accounting for detailed fiber orthotropy to capture the local heat flux fields in unidirectional graphite/epoxy composites.

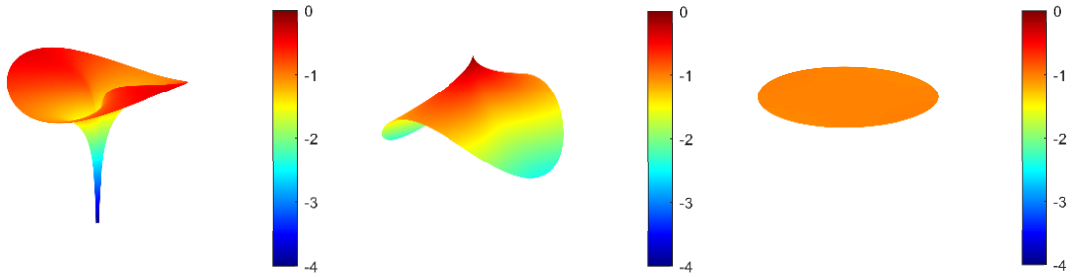

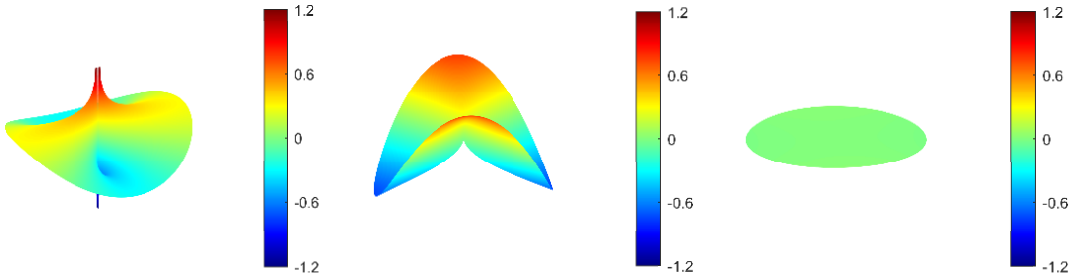

(d) (e) (f)

Figure 14 Comparison of NN-generated fiber heat flux $\left(\mathrm{W/m^2}\right)$ distributions under macroscopic temperature gradient $\bar{H}_2 = 1\mathrm{K/m}$: (a) q_2 distributions in RO fiber; (b) q_2 distributions in CO fiber; (c) q_2 distributions in TI fiber; (d) q_3 distributions in RO fiber; (e) q_3 distributions in CO fiber; (f) q_3 distributions in TI fiber

To examine the impact of collocation point distribution on neural network training and predictive performance, we consider square arrays of unidirectional CO fibers with 40% volume fraction. As shown in Figure 15, collocation points are distributed either randomly or uniformly on each exterior face of the unit cell and along the fiber-matrix interface to evaluate their influence. A biaxial temperature gradient of $\bar{H}_2 = 0.5\bar{H}_3 = 1\mathrm{K/m}$ is applied. Figure 16 compares the training loss functions for unit cells with randomly and uniformly distributed collocation points. The two loss functions remain nearly coincident up to approximately 6000 epochs. This indicates that, in the early and mid-stages of training, both NNs are able to learn the underlying solution effectively, regardless of the specific collocation point distribution. Beyond 6000 epochs, however, the loss function for the uniform distribution begins to converge slightly faster than that of the random distribution, suggesting that a more evenly spaced set of collocation points may facilitate smoother refinement of the solution in the later stages of training. Despite these differences, the heat flux fields achieved by both distributions are comparable, as shown in Figures 17-18, indicating that both random

and uniform point distributions can ultimately provide accurate training results. Once again, the FEM and NN results demonstrate excellent agreement within the matrix phase, whereas in the fiber phase, marked differences arise, primarily due to their varying ability to capture the singular heat flux field.

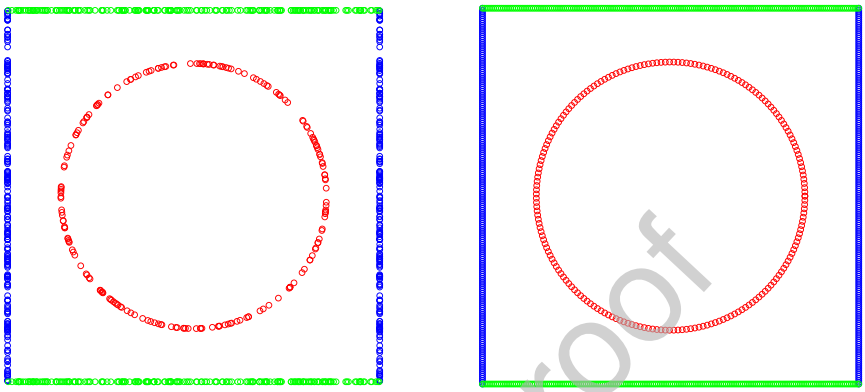

(a) (b)

Figure 15 Distributions of collocation points in faces of square unit cells with 40% volume fraction: (a) random distribution; (b) uniform distribution. It is noted that on the exterior faces, the collocation points are distributed periodically to enforce the periodicity boundary conditions.

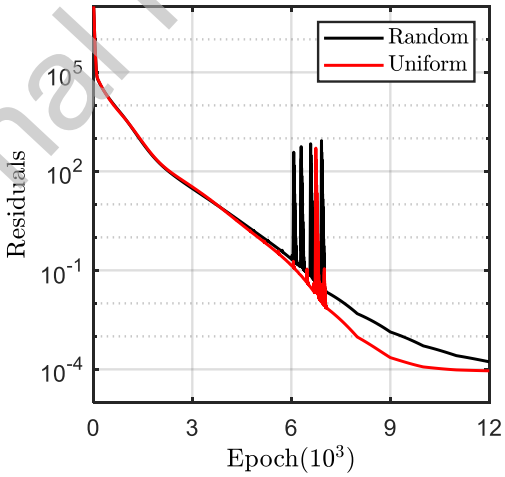

Figure 16 Comparison of training loss functions for unit cells with randomly and uniformly distributed collocation points

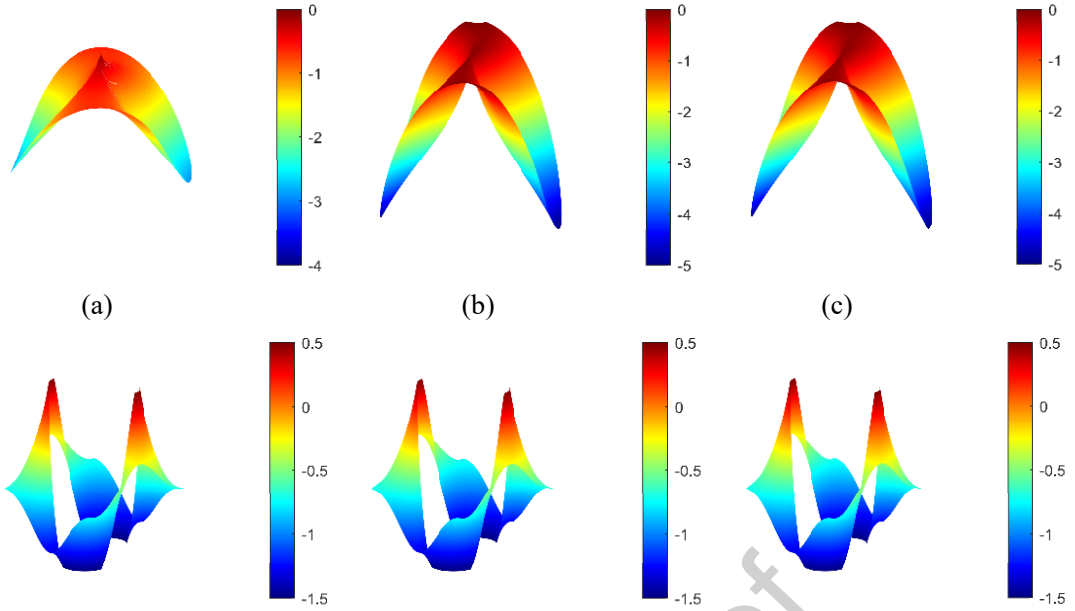

Figure 17 Heat flux $q_2\left(\mathrm{W/m^2}\right)$ distributions in square array of RO fiber under macroscopic temperature gradient $\bar{H}_2 = 0.5\bar{H}_3 = 1\mathrm{K/m}$: (a) fiber heat flux distributions obtained from FEM results; (b) fiber heat flux distributions obtained from NN with random collocation points; (c) fiber heat flux distributions obtained from NN with uniform collocation points; (d) matrix heat flux distributions obtained from FEM results; (e) matrix heat flux distributions obtained from NN with random collocation points; (f) matrix heat flux distributions obtained from NN with uniform collocation points

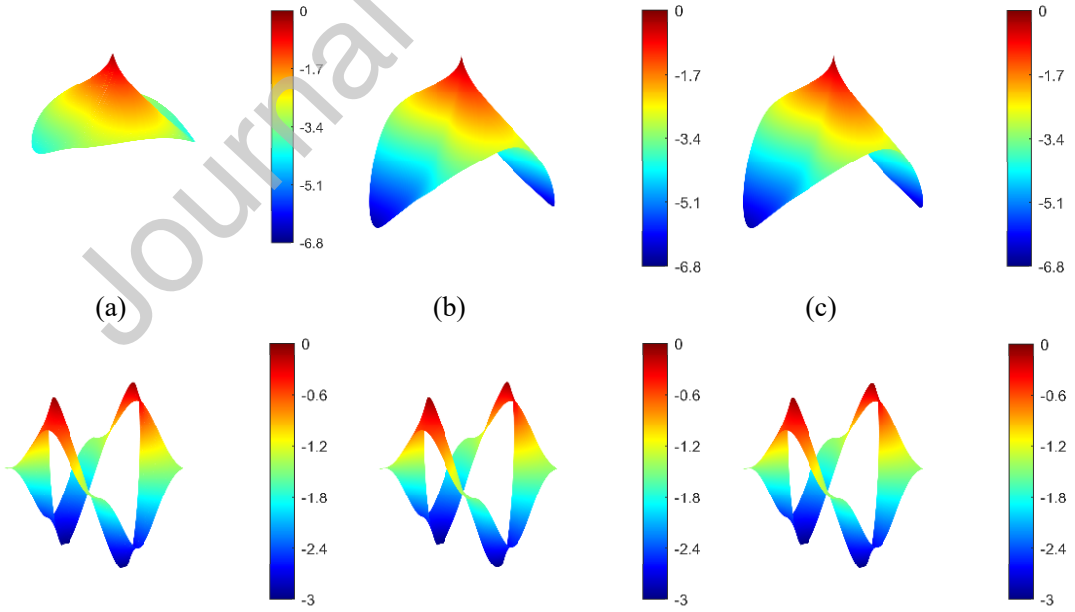

Figure 18 Heat flux $q_3\left(\mathrm{W/m^2}\right)$ distributions in square array of RO fiber under macroscopic temperature gradient $\bar{H}_2 = 0.5\bar{H}_3 = 1\mathrm{K/m}$: (a) fiber heat flux distributions obtained from FEM results; (b) fiber heat flux distributions obtained from NN with random collocation points; (c) fiber heat flux distributions obtained from NN with uniform collocation points; (d) matrix heat flux

distributions obtained from FEM results; (e) matrix heat flux distributions obtained from NN with random collocation points; (f) matrix heat flux distributions obtained from NN with uniform collocation points

4.3 Transfer learning

In this section, we demonstrate the feasibility of leveraging transfer learning to efficiently train a new unit cell model based on an existing pre-trained network model. The core idea is to apply the coefficients of harmonic eigenfunctions from a pretrained neural network model directly to the new network model with unseen geometry, rather than training the network from scratch.

To rigorously assess the validity of the transfer learning approach, we consider significantly different unit cell geometries. Specifically, we extract the coefficients of harmonic eigenfunctions for square arrays of RO fiber with 15% volume fraction, i.e., the source model, in Figure 11. These coefficients are then applied to a new neural network for a hexagonal array of RO fibers with a 30% volume fraction, namely, the target model. To minimize the significant updating of the coefficients of harmonic eigenfunctions, the initial learning rates are set to 1/10 of those used in the source model, whereas in the direct training model, the learning rates are kept the same as in Section 4.1. The evolution of loss values for direct training and transfer learning of the neural networks is presented in Figure 19. The transfer learning model was trained for 2000 epochs, whereas the direct training model was trained until the loss values stabilized and reached a comparable level (after around 9000 epochs). As anticipated, the transfer learning approach yields significantly faster loss convergence relative to the direct training process.

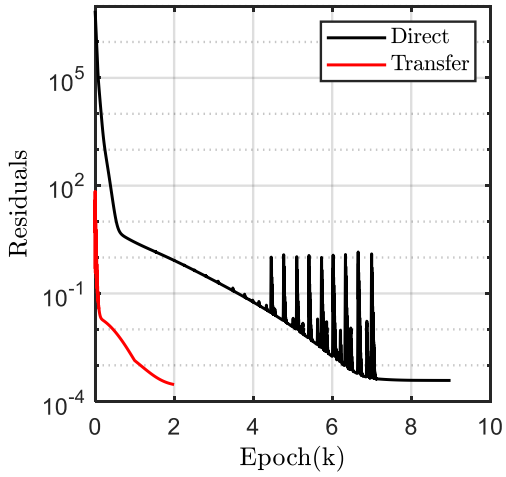

Figure 19 Comparison of loss functions for direct training and transfer learning model for hexagonal array of RO fibers with 30% volume fraction

The transverse heat flux distributions q_2 and q_3 for the fiber and matrix phases of the hexagonal arrays of RO fiber are shown in Figures 20-21, respectively. It is noted that the predictions from the transfer learning model show good correlation with the FEM and direct NN results. The complete set of the coefficients in the series expansion of fiber temperature, for the source model and the transfer learning model (i.e., the target model), is compared in Table 3. It is evident that these coefficients are of or nearly at the same order, demonstrating the similarity of the learning task. The success of transfer learning is rooted in the strong similarity between the source and target heat flux fields in square and hexagonal unit cells (Figures 12-13 and 20-21), respectively. The source network already captures the dominant temperature field characteristics, allowing the transfer model to converge quickly with minimal additional training, as the pre-trained harmonic term coefficients provide an appropriate starting point, avoiding random parameter initialization and reducing the coefficient discrepancy across different tasks.

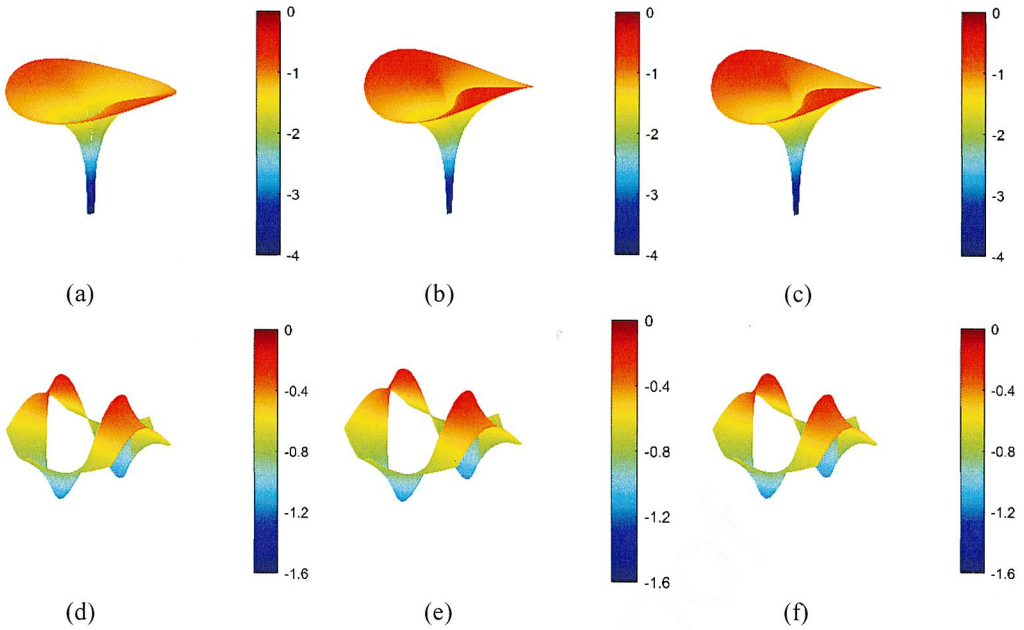

Figure 20 Heat flux $q_2\left(\mathrm{W/m^2}\right)$ distributions in hexagonal unit cell with RO fiber under macroscopic temperature gradient $\bar{H}_2 = 1\mathrm{K/m}$: (a) fiber heat flux distributions obtained from FEM results; (b) fiber heat flux distributions obtained from NN with transfer learning; (c) fiber heat flux distributions obtained from NN with direct training; (d) matrix heat flux distributions obtained from FEM results; (e) matrix heat flux distributions obtained from NN with transfer learning; (f) matrix heat flux distributions obtained from NN with direct training

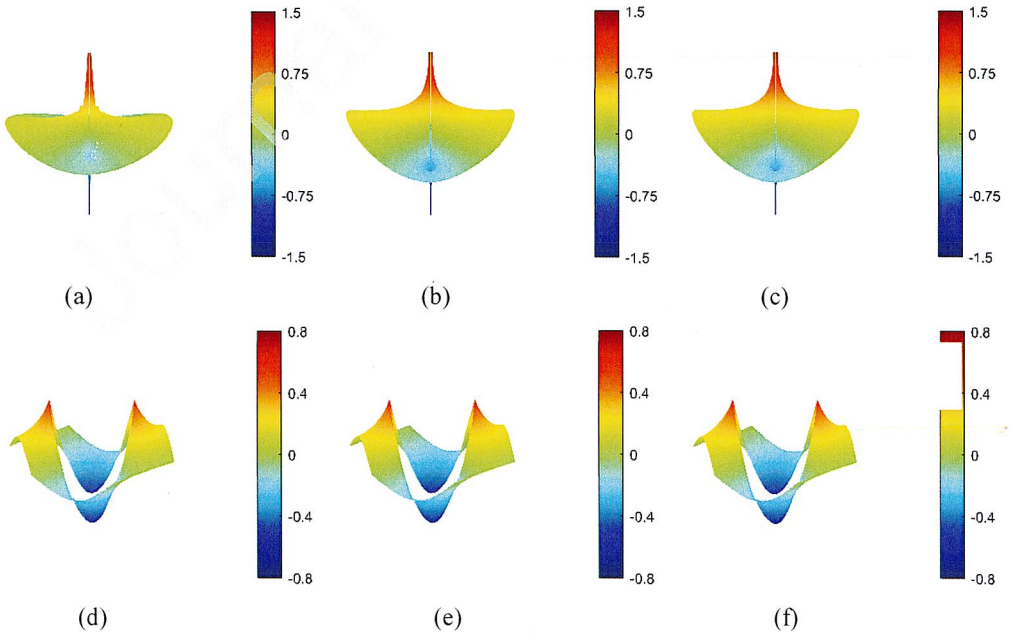

Figure 21 Heat flux $q_3\left(\mathrm{W/m^2}\right)$ distributions in hexagonal unit cell with RO fiber under macroscopic temperature gradient $\bar{H}_2 = 1\mathrm{K/m}$: (a) fiber heat flux distributions obtained from FEM results; (b) fiber heat flux distributions obtained from NN with transfer learning; (c) fiber heat flux distributions obtained from NN with direct training; (d) matrix heat flux distributions obtained from FEM results; (e) matrix

heat flux distributions obtained from NN with transfer learning; (f) matrix heat flux distributions obtained from NN with direct training

Table 3 Comparison of coefficients in the series expansion of fiber temperature obtained using the source and transfer learning models

	Source	Transfer		Source	Transfer
F_{11}^f	2.27050928e-01	2.61466079e-01	F_{12}^f	-8.03988246e-04	-1.41747191e-06
F_{21}^f	3.95436319e-07	1.69748174e-06	F_{22}^f	2.18678155e-05	-3.92104260e-07
F_{31}^f	1.31122896e-03	1.13392152e-05	F_{32}^f	3.78743125e-05	3.19823595e-07
F_{41}^f	1.32407593e-06	1.28429900e-06	F_{42}^f	1.09206035e-06	3.01591907e-07
F_{51}^f	-4.73763755e-05	-7.82133253e-04	F_{52}^f	4.82261519e-06	-2.80532027e-07
F_{61}^f	1.73242702e-06	1.00915973e-06	F_{62}^f	-1.39880378e-05	2.64276034e-07
F_{71}^f	9.26445788e-06	2.46395980e-04	F_{72}^f	-8.52790828e-08	-3.03139517e-07
F_{81}^f	-4.63086732e-07	1.13500048e-06	F_{82}^f	1.93864362e-07	-4.36299560e-08
F_{91}^f	-2.37822042e-06	-2.11048563e-06	F_{92}^f	-1.57188008e-08	-1.15327243e-07
$F_{10,1}^f$	3.10974921e-07	1.17659070e-06	$F_{10,2}^f$	2.48042184e-08	-7.97076603e-08

Table 4 presents comparison of the homogenized in-plane thermal conductivities $k_2^* = k_3^*$ obtained from the FEM simulations and the proposed NN model for different unit cell configurations and fiber volume fractions. While the local heat flux shows notable differences in the fiber phases, the homogenized in-plane thermal conductivities predicted by the NN and FEM remain in close agreement, indicating that the proposed model accurately captures the overall effective behavior.

Table 4 Comparison of the homogenized in-plane thermal conductivities $k_2^* = k_3^* \left(\mathrm{W \cdot m^{-1} \cdot K^{-1}}\right)$ obtained using the FEM and the proposed NN model

	Fiber volume fraction	NN	FEM	Relative error
Hexagonal unit cell with CO fiber	60%	1.4281	1.4276	0.04%
Square unit cell with CO fiber	60%	1.4700	1.4721	0.14%
Hexagonal unit cell with RO fiber	30%	0.8125	0.8160	0.43%
Square unit cell with RO	15%	0.6365	0.6365	0

5. Conclusions

In this study, a new periodic homogenization approach is presented for modeling steady-state heat conduction in periodic unidirectional composites with cylindrically orthotropic fiber phases, characterized by two-dimensional hexagonal and square repeating unit cells. The key contributions of the proposed method are two-fold: (1) the development of a new periodic micromechanics model that explicitly accounts for the cylindrical orthotropic fiber morphologies, enabling a faithful characterization of the complex heat conduction behavior of such composites; and (2) a simple yet effective neural network framework that enforces strictly the governing steady-state heat conduction equations while the continuity conditions of the temperature and heat flux at the fiber/matrix interface, in conjunction with the periodicity boundary conditions at the unit cell boundaries, are approximately satisfied through collocation points in the loss function.

The proposed micromechanics-informed neural network enables the accurate identification of the little explored temperature field and singular heat flux fields within the 2D RUCs containing radially and circumferentially orthotropic graphite fibers, even with only a limited number of harmonic eigenfunctions. The results show that fiber orthotropy produces markedly different heat flux distributions, which are validated against finite element simulations. In addition, transfer learning is demonstrated to be effective in accelerating convergence for new geometries. Although the present study is restricted to a steady-state conduction problem in 2D RUCs, the proposed framework is extensible for exploring fiber morphology effects under more general loading

conditions and in fully three-dimensional configurations.

CRediT authorship contribution statement

Ce Xiao Writing-original draft, Validation, Methodology, Investigation, Formal analysis. **Qiang Chen:** Writing-original draft, Visualization, Methodology, Investigation, Formal analysis, Supervision, Conceptualization, Funding acquisition. **Mohammed El Fallaki Idrissi:** Writing - review & editing, Validation, Methodology, Investigation. **Zhibo Yang:** Writing - review & editing, Validation, Methodology, Investigation, Funding acquisition. **Xuefeng Chen:** Writing - review & editing, Validation, Methodology, Investigation. **George Chatzigeorgiou:** Writing - review & editing, Validation, Methodology, Investigation. **Fodil Meraghni:** Writing - review & editing, Validation, Methodology, Investigation.

Acknowledgment

Qiang Chen acknowledges the financial support of the National Key Research and Development Program of China (Grant No. 2024YFB4609000) and the National Natural Science Foundation of China (Grant No. 52505126). Zhibo Yang acknowledges the financial support of the National Natural Science Foundation of China (Grant No. 92360306).

References

[1] S. Tang, C. Hu, Design, Preparation and Properties of Carbon Fiber Reinforced Ultra-High Temperature Ceramic Composites for Aerospace Applications: A Review, J. Mater. Sci. Technol., 33 (2017) 117-130.

[2] X. Huang, Fabrication and Properties of Carbon Fibers, Materials, 2 (2009) 2369-2403.

[3] W.B. Avery, C.T. Herakovich, Effect of Fiber Anisotropy on Thermal Stresses in Fibrous Composites, J. Appl. Mech., 53 (1986) 751-756.

[4] Z. Hashin, Thermoelastic properties and conductivity of carbon/carbon fiber composites, Mech. Mater., 8 (1990) 293-308.

[5] T. Chen, G.J. Dvorak, Y. Benveniste, Stress fields in composites reinforced by coated cylindrically orthotropic fibers, Mech. Mater., 9 (1990) 17-32.

[6] G. Chatzigeorgiou, F. Meraghni, N. Charalambakis, et al., Multiscale modeling accounting for inelastic mechanisms of fuzzy fiber composites with straight or wavy carbon nanotubes, Int. J. Solids Struct., 202 (2020) 39-57.

[7] Q. Chen, G. Chatzigeorgiou, F. Meraghni, Hybrid hierarchical homogenization theory for unidirectional CNTs-coated fuzzy fiber composites undergoing inelastic deformations, Compos. Sci. Technol., 215 (2021) 109012.

[8] G. Wang, M.-J. Pindera, Locally Exact Homogenization of Unidirectional Composites With Cylindrically Orthotropic Fibers, J. Appl. Mech., 83 (2016).

[9] G. Wang, M. Gao, B. Yang, et al., The morphological effect of carbon fibers on the thermal conductive composites, Int. J. Heat Mass Transf., 152 (2020) 119477.

[10] A.S. Drago, M.-J. Pindera, A Locally Exact Homogenization Theory for Periodic Microstructures With Isotropic Phases, J. Appl. Mech., 75 (2008).

[11] X. Du, Q. Chen, G. Chatzigeorgiou, et al., Nitsche's Method Enhanced Isogeometric Homogenization of Unidirectional Composites with Cylindrically Orthotropic Carbon/Graphite Fibers, Compos. Sci. Technol., 256 (2024) 110787.

[12] M. Raissi, P. Perdikaris, G.E. Karniadakis, Physics-informed neural networks: A deep learning framework for solving forward and inverse problems involving nonlinear partial differential equations, J. Comput. Phys., 378 (2019) 686-707.

[13] H. Saidaoui, L. Espath, R. Tempone, Deep NURBS—admissible physics-informed neural networks, Eng. Comput., 40 (2024) 4007-4021.

[14] J. Yu, L. Lu, X. Meng, et al., Gradient-enhanced physics-informed neural networks for forward and inverse PDE problems, Comput. Methods Appl. Mech. Eng., 393 (2022) 114823.

[15] E. Haghighat, M. Raissi, A. Moure, et al., A physics-informed deep learning framework for inversion and surrogate modeling in solid mechanics, Comput. Methods Appl. Mech. Eng., 379 (2021) 113741.

[16] E. Samaniego, C. Anitescu, S. Goswami, et al., An energy approach to the solution of partial differential equations in computational mechanics via machine learning: Concepts, implementation and applications, Comput. Methods Appl. Mech. Eng., 362 (2020) 112790.

[17] G.E. Karniadakis, I.G. Kevrekidis, L. Lu, et al., Physics-informed machine learning, Nat. Rev. Phys., 3 (2021) 422-440.

[18] J.D. Toscano, V. Oommen, A.J. Varghese, et al., From PINNs to PIKANs: recent

advances in physics-informed machine learning, Mach. Learn. Comput. Sci. Eng., 1 (2025) 15.

[19] A. Henkes, H. Wessels, R. Mahnken, Physics informed neural networks for continuum micromechanics, Comput. Methods Appl. Mech. Eng., 393 (2022) 114790.

[20] X. Ren, X. Lyu, Mixed form based physics-informed neural networks for performance evaluation of two-phase random materials, Eng. Appl. Artif. Intell., 127 (2024) 107250.

[21] H. Guo, X. Zhuang, P. Chen, et al., Analysis of three-dimensional potential problems in non-homogeneous media with physics-informed deep collocation method using material transfer learning and sensitivity analysis, Eng. Comput., 38 (2022) 5423-5444.

[22] W. Wu, M. Daneker, K.T. Turner, et al., Identifying Heterogeneous Micromechanical Properties of Biological Tissues via Physics-Informed Neural Networks, Small Methods, 9 (2025) 2400620.

[23] J. Jiang, J. Wu, Q. Chen, et al., Physically informed deep homogenization neural network for unidirectional multiphase/multi-inclusion thermoconductive composites, Comput. Methods Appl. Mech. Eng., 409 (2023) 115972.

[24] J. Wu, J. Jiang, Q. Chen, et al., Deep homogenization networks for elastic heterogeneous materials with two- and three-dimensional periodicity, Int. J. Solids Struct., 284 (2023) 112521.

[25] J. Linghu, W. Gao, H. Dong, et al., High-order multi-scale neural network method for quasi-static thermo-mechanical problems of composite materials, Appl. Math. Model., 148 (2025) 116232.

[26] J.-Q. Tarn, Stress Singularity in an Elastic Cylinder of Cylindrically Anisotropic Materials, J. Elasticity, 69 (2002) 1-13.

[27] S.C. Cowin, M. Fraldi, On singularities associated with the curvilinear anisotropic elastic symmetries, Int. J. Non-Linear Mech., 40 (2005) 361-371.

[28] Q. Chen, W. Tu, J. Wu, et al., Elasticity-inspired data-driven micromechanics theory for unidirectional composites with interfacial damage, Eur. J. Mech. A/Solids, 111 (2025) 105506.

[29] M.-J. Pindera, H. Khatam, A.S. Drago, et al., Micromechanics of spatially uniform heterogeneous media: A critical review and emerging approaches, Compos. B Eng., 40 (2009) 349-378.

[30] Z. Yang, M. Li, Y. Sun, et al., A second-order reduced homogenization for nonlinear structures with periodic configurations in cylindrical coordinates, Appl. Math. Model., 119 (2023) 1-26.

[31] Y. Benveniste, T. Chen, G.J. Dvorak, The effective thermal conductivity of composites reinforced by coated cylindrically orthotropic fibers, J. Appl. Phys., 67 (1990) 2878-2884.

[32] Q. Chen, G. Wang, M.-J. Pindera, Homogenization and localization of nanoporous composites-A critical review and new developments, Compos. B Eng., 155 (2018) 329-368.

[33] L.D. McClenny, U.M. Braga-Neto, Self-adaptive physics-informed neural networks, Comput. Phys., 474 (2023) 111722.

[34] J. Wu, Q. Chen, J. Jiang, et al., Adaptive deep homogenization theory for periodic heterogeneous materials, Compos. Struct., 340 (2024) 118171.

Declaration of interests

☒ The authors declare that they have no known competing financial interests or personal relationships that could have appeared to influence the work reported in this paper.

☐ The authors declare the following financial interests/personal relationships which may be considered as potential competing interests: